Journal of Nuclear Materials 466 (2015) 539–550

Contents lists available at ScienceDirect

Journal of Nuclear Materials

journal homepage: www.elsevier.com/locate/jnucmat

Energetics and electronic structure of UAl_4 with point defects

L. Kniznik [a, b], P.R. Alonso [a, b], P.H. Gargano [a, b], G.H. Rubiolo [a, b, c, *]

[a] Gerencia Materiales, Comisión Nacional de Energía Atómica, Av. Gral. Paz 1499, B1650KNA, San Martín, Buenos Aires, Argentina
[b] Instituto de Tecnología J. Sabato, CNEA – UNSAM, Av. Gral. Paz 1499, B1650KNA, San Martín, Buenos Aires, Argentina
[c] CONICET, Av. Rivadavia 1917, 1033, CABA, Argentina

ARTICLE INFO

Article history:
Received 20 May 2015
Received in revised form
20 August 2015
Accepted 25 August 2015
Available online 29 August 2015

Keywords:
Actinide materials and compounds
DFT calculations
Crystal structure
Electronic properties
Point defects

ABSTRACT

UAl_4 ideal and defect structures were studied within the framework of the Density Functional Theory. The structural and magnetic ordering of UAl_4 in paramagnetic, ferromagnetic, and antiferromagnetic states have been investigated, within the collinear and non-collinear spin approximation, using the GGA model, as embedded in the program package VASP. An antiferromagnetic $(0\bar{1}1)$ layer structure with spins aligned to the [010] direction was found to be energetically preferred. The analysis of density of states and bonding charge density point out that the bonding mechanism consists primarily of band mixing between the U 5f and Al 3p states. Supercells were built from UAl_4 unit cells with the established magnetic structure. For those supercells we calculated the energy of formation of vacancies and antisite defects taking into account the existence of three distinct aluminum sites. Point defect formation energies, local lattice relaxations, as well as the defect induced magnetic ordering and electronic density redistribution, are discussed. It is shown that antiferromagnetism is locally broken. Al antisites and U antisites in Al 4e Wyckoff positions are the constitutional point defects in Al-rich and U-rich oI20 UAl_4, respectively. In this way we have presented here the first set of data which makes it possible to discuss and quantify the point defects concentrations in the experimental composition range for existence of this uranium aluminide.

1. Introduction

Fuel cores for nuclear research and test reactors are aluminum matrix composites constituted of uranium alloys such as UAl_x (mainly UAl_3) or U_3Si_2 dispersed in aluminum powder [1,2]. γ-U(Mo) alloys are now considered as the most promising candidates for the fuel core conversion of those research and test reactors currently using highly-enriched uranium (HEU) to low-enriched uranium (LEU) [3,4]. Therefore, reactions between U alloys and Al alloys are of great technical interest. The U–Al binary system has been extensively studied; it comprises three intermetallic compounds, viz. UAl_2, UAl_3, and UAl_4 ([5] and references therein). The presence of Mo in U introduces a complexity to the interdiffusion behavior of U vs. Al, the reaction product formed at the interface consists of UAl_3, UAl_4, $U_6Mo_4Al_{43}$ and UMo_2Al_{20} and is stratified in three main zones, two of which present a periodic layered morphology [6,7]. The layer close to the Al side consists essentially of the UAl_4 phase associated with the UMo_2Al_{20} phase. In the thicker layer close to U–Mo only $U_6Mo_4Al_{43}$ and UAl_3 phases are identified. The observed growth kinetics of the reaction product and its global energy of activation are very close to that found for the U/Al binary system despite the fact that the UMo_2Al_{20} and $U_6Mo_4Al_{43}$ ternary phases appear in the interaction zone. This means that the presence of these ternary phases has no significant influence neither on the growth kinetics of the reaction product nor on its activation energy [7,8]. Besides, as these alloys are intended as fuel for research reactors, the interdiffusion products between U(Mo) and Al must be considered according to their performance under irradiation conditions. In this context, swelling is produced that has been related to the formation of amorphous phases [9]. While UAl_3 appeared as a crystallized phase under heavy ion irradiation [10], and early works recommended to suppress UAl_4 formation [11], recent research enlightens the effect of product formation on fuel performance. Recently, it has been pointed out that amorphization or crystallinity results from the joint effect of composition (or Al/(U + Mo) ratio), irradiation temperature, and fission rate [12]. Finally, there is now convincing experimental evidence that the radiation performance of $U_6Mo_4Al_{43}$ phase, at an

* Corresponding author. Gerencia Materiales, Comisión Nacional de Energía Atómica, Av. Gral. Paz 1499, B1650KNA, San Martin, Buenos Aires, Argentina.
E-mail address: rubiolo@cnea.gov.ar (G.H. Rubiolo).

http://dx.doi.org/10.1016/j.jnucmat.2015.08.049
0022-3115/

irradiation temperature of 200 °C and up to 100 dpa, is significantly worse than that of UMo_2Al_{20} and UAl_4 [13]. Moreover, the UAl_4 phase retains crystallinity, no large voids or bubbles are found and the development of dislocation structure is noticeable suggesting a possible annealing effect by irradiation at a high homologous temperature.

Concerning the formation in the interdiffusion process and the irradiation behavior, the study of point defect structure of the UAl_4 lattice is mandatory. A survey of literature evidences some controversies about this issue. Chemical analysis by Borie [14] showed that the composition range for existence of this compound may be between 81.8 and 83.1 at% Al, although the symmetry revealed by X-ray measurements suggested that the formula could be UAl_4. Borie [14] explained the inconsistency by assuming that some uranium sites are unoccupied or occupied by aluminum atoms. Other works followed that either confirmed that narrow composition range [15] or gave a composition value of $U_{0.9}Al_4$ (81.6 at% Al) [16]. Elevated temperature electrical conductivity data by Jesse et al. [17] suggested a wide homogeneity range for UAl_4 from 80.0 to 82.8 at% Al. However, Rietveld refinements of high quality experimental X-ray diffraction powder pattern show that UAl_4 would form as a fully stoichiometric compound without constitutional defects in the U sublattice [18]. Measured enthalpies of formation of the whole set of compounds existing in the U–Al binary system [19] also account for the stability of the UAl_4 compound within experimental uncertainties. Currently, UAl_4 is assessed as an aluminum enriched compound with a homogeneity range between 80 and 82.8 at% Al which forms by a peritectic reaction between UAl_3 and liquid Al at 732 °C and a composition of 81.8 at% Al [5]. It has an orthorhombic D1b structure (oI20, spatial group 74) exhibiting a polymorphic transformation $UAl_4(\beta) \leftrightarrow UAl_4(\alpha)$ at 646 °C [20].

The formation energies of both stoichiometric compound and off-stoichiometric compound containing point defects can nowadays be obtained from ab-initio electronic structure calculations based on density functional theory (DFT) [21,22]. In the case of an imperfect crystal the calculations must be performed on large supercells containing one defect, either a vacancy or an antisite [23]. These formation energies are used to evaluate the formation energies of the point defects.

In a first study, we determined from first-principles the formation energy of the intermetallic compounds which are present in the U–Al system. Spin polarized calculations through the all electrons method implemented in the Wien2k code [24] failed to predict experimental stabilities [25]. An agreement with existent ground state was obtained [26] through new spin polarized calculations adding spin orbit coupling (SOC) within a pseudopotentials method implemented in the VASP code [27]. However, formation energy values appear underestimated. A better agreement with experimental values was obtained by other authors [28] through ab initio calculations (Wien2k code) that use experimental values for lattice parameters together with SOC. This feature alerts us about the possibility of a discrepancy between stoichiometric optimized compound through ab initio methods and real compound, since experimental values for lattice parameters already comprises the information of possible defect structure.

In a second work, we reported preliminary results of the vacancies and antisites defects formation energies in the UAl_4 phase [29]. Only one of the three inequivalent aluminum sites was considered. These results led to the conclusion that antisite defects could be stabilized with respect to vacancies in aluminum rich UAl_{4+x}. Even so, a thorough theoretical study of defect structure that could correctly describe experimental findings was still lacking.

While stability is a consequence of electronic and magnetic configuration, these features have been scarcely experimentally investigated in the case of UAl_4. At low temperatures, the specific heat of UAl_4 follows the equation $C = \gamma T + \beta T^3$ where the first term is an electronic contribution and the second term is the phonon contribution. The γ value and the Debye temperature θ_D in UAl_4 were determined to be 89 mJ/(K^2 mol) and 275 K, respectively [30,31]. The electrical resistivity decreases with decreasing temperatures from room temperature, with a convex curvature. At low temperatures, the resistivity follows the quadratic temperature dependence, namely $\rho = \rho_0 + AT^2$, indicating the Fermi liquid behavior. With this data and the so-called Kadowaki–Woods relation [32], a specific heat coefficient of 100 mJ/(K^2 mol) was estimated close to the experimental result of specific heat measurement [33,31]. All the magnetic susceptibilities measured with the magnetic field parallel to the crystal axes increase with decreasing temperatures and have a broad maximum around 100 K. The anisotropy is relatively small [31]. A Curie–Weiss behavior is evidenced at T > 400 K with an effective magnetic moment $\mu_{eff} = 3.8\ \mu_B$ and a paramagnetic Curie temperature $\theta_C = -185$ K [34]. From all these results, it is considered that UAl_4 possesses the itinerant nature of 5f electrons at low temperatures. The complex magnetic behavior was discussed in terms of the spin fluctuation model [33,35] but its paramagnetic or antiferromagnetic character is not yet resolved. Regarding experimental research on bonding that results from electronic configuration, X-ray and ultra-violet photoelectron spectroscopy measurements on U overlayers on Al substrate have proved that interactions between U atoms and Al atoms are stronger than those among U atoms in the overlayer [36]. The evaluation of electronic structure and bonding in UAl_x compounds from DFT is only found in literature for x = 2 and 3 [37–41], and magnetic configuration has not been theoretically analyzed for none of the UAl_x compounds. First-principles modeling of point defects formation energies has been performed for uranium oxide nuclear fuels (for nuclear power reactors) over several decades [42–46]. Conversely, for uranium aluminide, there are not first principles simulations up to date.

In this paper, the magnetic ordering of UAl_4 in paramagnetic, ferromagnetic, and antiferromagnetic states has been investigated, within the collinear and non-collinear spin approximation, using the GGA model, as embedded in the program package VASP. The magnetic structure with the lowest energy state was found and its magnetocrystalline anisotropy was studied taking into account the SOC. The electronic structure and nature of bonding was analyzed as obtained without SOC. Supercells were built from UAl_4 unit cells with the determined magnetic structure. These supercells were used to estimate the energy of formation of vacancies and antisite defects in UAl_4 taking into account the existence of three distinct aluminum sites. Ab-initio calculations of defect structures were performed allowing structural relaxations in atomic positions and without SOC. Finally, we discuss the electronic structure around the defect site using the electronic density of states and charge-density maps.

The paper is organized as follows. In Section 2, the method and the calculation details are described. In Section 3 we present and discuss our results, concerning the crystal, electronic and magnetic structure of the perfect UAl_4 crystal and the formation energies, the structural relaxations and the electronic structure of the constitutional point defects in UAl_4. Finally, conclusions are summarized in Section 4.

2. Calculation methods

All density functional theory (DFT) [21,22] calculations in the present work were performed by means of the Vienna Ab initio Simulation Package (VASP) [27], making use of the Projector

Augmented Waves (PAW) technique [47]. For the exchange correlation functional, the generalized gradient approximation (GGA) as parameterized by Perdew, Burke and Ernzerhof (PBE) [48] was applied.

The calculations included fourteen valence electrons for U ($6s^2 6p^6 5f^3 6d^1 7s^2$) and three valence electrons for Al ($3s^2 3p^1$) with a plane-wave cutoff energy of 600 eV for both elements.

In order to determine the magnetic ground state, it was necessary to perform collinear and non-collinear spin calculations. The non-collinear calculations were performed using the fully unconstrained approach included in the VASP package [49]. The method allows both the atomic and magnetic structures to relax simultaneously and self-consistently and the magnetization density is described as a continuous vector variable of position. The collinear and non-collinear calculations can predict the set of directions for the spins of the magnetic ground state but this set of directions is unrelated to the underlying crystal lattice. This can be accomplished when spin–orbit coupling (SOC) is added to the Hamiltonian [50]. Therefore, in order to evaluate magnetic anisotropies, we computed the total energy of the magnetic ground state with different orientations of magnetization including SOC.

The k-point meshes for Brillouin zone sampling are constructed using the Monkhorst–Pack scheme. In the case of the stoichiometric oI20 UAl_4 unit cell, total energy convergence with the number of k-points was investigated with $M \times M \times M$ (odd number) grids up to $M = 13$ using lattice parameters and ionic position from experimental data. The energy convergence was reached to less than 0.0003 eV/cell for $M \geq 9$. After that, all geometry relaxation was performed with a $9 \times 9 \times 9$ k-points grid allowing ionic and cell shape relaxation and cell volume optimization.

To determine the formation energies of isolated point defects we used both a 80-atom $2 \times 2 \times 1$ supercell and a larger 120-atom $3 \times 2 \times 1$ supercell, each containing one single point defect (vacancy or antisite) per supercell. In all these cases, calculations were performed with a $3 \times 3 \times 3$ k-points grid. To take into account the effects of local atomic relaxations around point defects, the internal coordinates of atom positions were allowed to relax within each supercell while the structure remained orthorhombic without changes in its volume and shape. The later was accomplished by using a conjugate-gradient scheme until the forces acting on the atoms were less than 0.01 eV/Å.

VESTA software (Visualization for Electronic and STructural Analysis, 3.1.8 version) [51] was used for valence electron density plots and visualization of structural models.

In studies of actinide based materials, one has to be careful also with the 5f electron correlation effect in addition to the SOC effect. The electronic density of states at both sides of the Fermi level can be obtained using X-ray photoelectron spectroscopy (XPS) and bremsstrahlung isochromat spectroscopy (BIS) [52]. The combination of these two methods allows a direct determination of both occupied (XPS) and empty (BIS) states. For rare earth metals it is well established that the combination of BIS and XPS spectra is split into two peaks separated by the Coulomb repulsion, U_{ff}, between 4f electrons [53,54]. The same explanation was done for the combined BIS and XPS spectra of 5f electrons in the light actinide (Th, U, and Np) dioxides [55–57]. The conventional DFT schemes that apply the GGA approximation underestimate the strong on-site Coulomb repulsion of the *f* electrons and consequently fail to capture the behavior mentioned above. It was only with the development of the GGA + U_{ff} approximation [58] and hybrid functionals [59,60] that the pure GGA failures in calculations of rare earth metals and actinide dioxides could be corrected. For uranium intermetallics the experimental situation is much different. Typically, separated peaks are not observed and in uranium metal [61], for example, the total observed f width is comparable to the one-electron width obtained in band calculations. Searching through the literature we could find only two publications where the GGA + U_{ff} methodology was applied to α-U, a $U_{ff} \approx 0.5$ *eV* parameter is empirically determined by fitting to existing experimental lattice constants in one case [62] and the cohesive energy in the other [63]. In the last paper there is also a comparison between calculated DOS and XPS-BIS spectra as a function of U_{ff} which show a mild modification with the inclusion of the Coulomb repulsion. The only reported combined XPS-BIS spectra for the uranium aluminides is that of UAl_2 [64]. The most striking feature is that the measured widths of the 5f spectral weights exceed the one-electron ones [37,38]. However, new literature about ab initio studies of UAl_2 have not tested the DFT + U approach to the best of our knowledge, for example see Refs. [41,65]. It is generally agreed that the actinide–actinide separation could enhance the localization of 5f electrons then diluting uranium atoms in a periodic cell should result in a wider density of states. The alloy system $U_xY_{1-x}Al_2$ has the same crystal structure for all x [66] and the 5f spectral weights for x = 0.1, 0.02 have been measured by XPS [67]. The major features of the spectra of these dilute systems are identical to those for x = 1, showing that the dilution of the uranium atoms in uranium aluminides does not result in narrower 5f band. We thus conclude that the DFT + U treatment, while essential for the strongly correlated insulating uranium oxide compounds, is at least difficult to validate against experimental data for the more weakly correlated uranium aluminides.

3. Results and discussion

3.1. Perfect UAl_4 crystal

3.1.1. Crystal structure

We begin by discussing the relative stability of the nonmagnetic (NM), collinear ferromagnetic (F) and antiferromagnetic (AF) phases of UAl_4. Fig. 1 shows the UAl_4 unit cell in F and three AF arrangements of the magnetic moments on the U atoms in the 4e sites. For all these magnetic phases the crystalline structure has been optimized independently. The calculated total energies are summarized in Table 1. The lowest energy state of the system is found for the AF(I) type magnetic structure.

The corresponding equilibrium lattice parameters, bulk modulus, and their fractional atomic coordinates are compared with available experimental values in Table 2.

The calculated equilibrium volume for the UAl_4 AF(I) structure differs by only 0.7% from the experimental volume; however the axial ratios c/a and c/b differ by 1.5% showing that the shape of the unit cell is more elongated in the c direction and contracted in the other two perpendicular directions. These results have consequences in the interatomic distances (see Table 3) with emphasis on U–U distances since the shortest distance from experimental data is reported between U^{I} and U^{IV} atoms whereas calculations predict it would occur between two U^{I} atoms equivalent through translation. Distances between U atoms were identified as a major factor in the magnetic nature of the material [69], due to its incidence in the overlapping of 5f bands between nearest atoms. As the distance is increased, the overlap decreases together with f bandwidth and the magnetism is stabilized. The limit value proposed by Hill is 3.4 Å. However, as both experimental and theoretical values are far larger than the 3.4 Å limit, the differences cannot explain the degree of itinerancy or localization of the 5f-electrons and the concomitant magnetic response in our calculation. The results on U–Al distances are also affected but the relative ordering is kept. The theoretical values are smaller than the experimental ones. Following the Koelling's criterion for the f-ligand hybridization [69], we hence have to expect a stronger hybridization between the

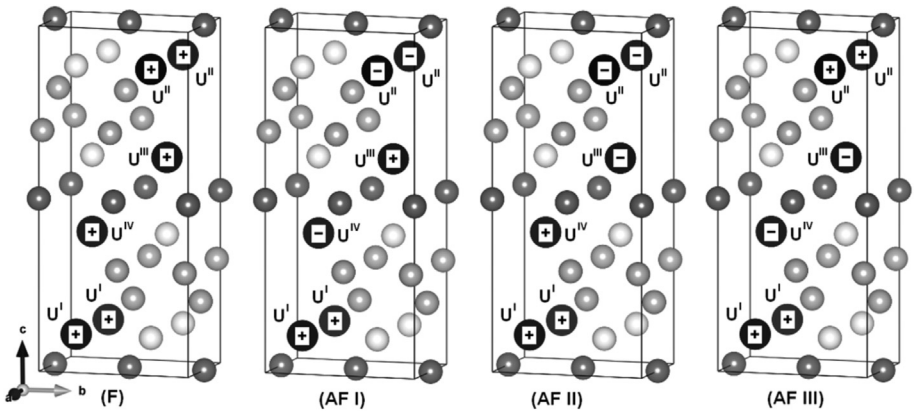

Fig. 1. Crystal structure and spin configurations for UAl_4. Black circles denote the U positions; circles colored with different gray shades indicate the positions of the different sites of Al atoms. Plus and minus signs indicate opposite directions of spins.

Table 1
Total (E) and relative (ΔE) energies per unit cell (UAl_4) for the magnetic structures shown in Fig. 1.

Structure	E (eV)	ΔE (eV)
NM	−106.5813	0.7491
F	−107.0812	0.2492
AF(I)	−107.3304	0
AF(II)	−107.1354	0.195
AF(III)	−107.2544	0.076

Table 2
Calculated structure parameters and bulk modulus for the AF(I) magnetic structure. The values in parentheses are experimental data from indicated references.

Lattice parameters (Å) [18]		a = 4.3738 (4.4014)		
		b = 6.2118 (6.2552)		
		c = 13.8413 (13.7279)		
Bulk modulus (GPa) [68]		88 (73 ± 5)		
Fractional atomic coordinates [18]				
	Wyckoff position	x	y	z
U(1)	4e	0	1/4	0.1119 (0.1130)
Al(1)	8h	0	0.0239 (0.0303)	0.6989 (0.6983)
Al(2)	4e	0	1/4	0.8898 (0.8891)
Al(3)	4b	0	0	0.5

Table 3
Selected interatomic distances (Å) for the AF(I) magnetic structure. The values in parentheses are experimental data from Ref. [18].

$U^{I}(1) - U^{IV}(1)$	4.4050 (4.3579)	U(1) − Al(1) × 4	3.021 (3.048)
$U^{IV}(1) - U^{III}(1)$	4.3860 (4.4054)	U(1) − Al(2)	3.0742 (3.074)
$U^{I}(1) - U^{I}(1)$	4.3738 (4.4014)	U(1) − Al(3) × 4	3.0973 (3.1137)

U 5f states and the Al 3p states in the theoretical results than in the experimental evidences.

3.1.2. Electronic structure

Previous density of states plots obtained through DFT based calculation methods were performed by Kang et al. [41] for UAl_x (x = 2,3) compounds, who suggested that chemical bonds are primarily formed between uranium and aluminum atoms, due to the strong hybridization between the U 5f states and the Al 3p states. The mentioned compounds have all cubic based structures. The higher aluminum content corresponds to UAl_3 compound. Its fcc structure with equal next nearest neighbor (NNN) distances between Al–Al atoms and between U–Al atoms (2.996 Å), is possible because of 12-atom coordination leaving one U atom surrounded by smaller Al atoms in spite of size mismatch. At higher aluminum composition, as in the case of UAl_4 phase, fcc structure cannot allocate Al atoms in a high symmetry configuration and a phase transition must occur to orthorhombic configuration. Though NNN number decreases and NNN distance between U atoms and Al atoms increases to 3.048 Å in the UAl_4 phase, the strong U–Al bond (p-d and p-f hybridization) given in UAl_3 should be maintained but weakened with farther aluminum atoms.

A method for studying the spatial distribution of chemical bonds is to calculate the bonding charge density (BCD). The BCD is defined as the difference between the self-consistent charge density of the interacting atoms in the compound and a reference charge density constructed from the superposition of the non-interacting atomic charge density at the crystal sites [70]. This quantity characterizes the redistribution of electrons that occurs when a crystal is formed from atoms being moved from infinity to their equilibrium positions. The calculation of BCD is only one of the methods to extract chemical information from the total electron density. Other types of difference function are also possible, but these are not discussed here.

To illustrate these bonding characteristics in the AF(I) structure of UAl_4 we use the charge density projected onto lattice planes which contain atomic sites of first, second and third nearest neighbors (see Fig. 2).

Fig. 3 shows the positive part of the BCD on the planes $(\bar{5}\ 0\ 27)$; $(\bar{2}\ 0\ 9)$; (100) and (010).

The BCD shows a depletion of the electronic density at the aluminum lattice sites accompanied by significant anisotropic buildup of the directional f-bonding charge at the uranium sites. From Fig. 3(a), the bonding charge accumulation at the U site is mainly along the U–Al directions. One can also see that there is a significant buildup of interstitial bonding charge at Al(1)-U-Al(2), Al(2)-U-Al(3) and Al(3)-U-Al(3) triangular bonding areas showing that the covalent character of the bonding between U and Al atoms is dominant. This feature should be consistent with a p-f hybridization. Indeed, it is evident that the interstitial bonding charge around the NNN Al(1) atoms exhibits lobes oriented along [010] direction indicating a strong degree of covalency as a consequence of p–p hybridization between them. Fig. 3(c) clearly shows that no bonding exists between nearest neighbor (NN) U atoms as expected due to the large distance between them. The (100) slice (Fig. 3(b)) gives other view of the bonding between U and its NN Al atoms completing the picture of the multicenter bonding which provides the interlayer cohesion to the structure.

Although a BCD plot can reveal valuable information about

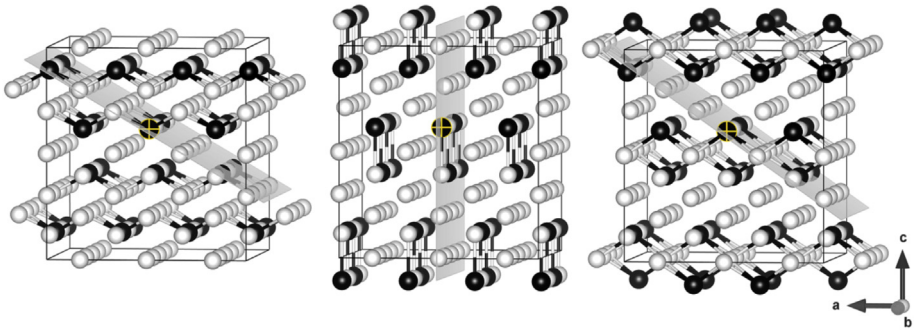

Fig. 2. Supercells (120 atoms) showing nearest neighbor bonds to the marked U atom on selected planes: (a) next nearest neighbors on plane $(\bar{5}\ 0\ 27)$; (b) Second nearest neighbors on plane (100); (c) Third nearest neighbors on plane $(\bar{2}\ 0\ 9)$, slightly tilted with respect to $(\bar{5}\ 0\ 27)$ plane. The Miller indices correspond to the unit cell of UAl_4. U and Al atoms are represented as black and white spheres respectively. First, second and third nearest neighbor bonds are shown as sticks.

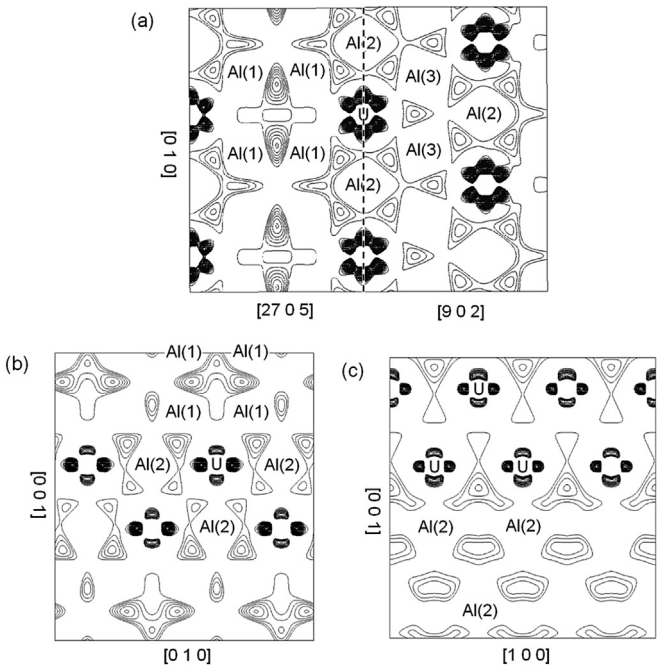

Fig. 3. BCD plot onto selected planes of UAl_4: (a) $(\bar{5}\ 0\ 27)$ and $(\bar{2}\ 0\ 9)$; (b) (100); (c) (010). Contourlines are drawn from 1×10^{-3} to 40×10^{-3} electrons/Å^3 with an interval of 1×10^{-3}.

regions of space having covalent bonding, the bonding nature of solids is better illustrated by partial density of state (PDOS) analysis [71]. The site projected PDOS plots of the UAl_4 NM and AF(I) structures are shown in Fig. 4(a) and (b) respectively. Only the contributions arising from U 6d, U 5f, and Al 3p states (for the three inequivalent sites) are presented since these are the ones relevant to our discussion.

The well defined peaks in Fig. 4(a) reveal an ordered structure. The states below 7.2 eV are mostly of the U 6d and Al 3p character and those lying above this energy belong mainly to the U 5f electronic bands. A strong hybridization between U 6d and Al 3p states is evident in the whole energy range and above 7.2 eV the Al 3p bands also participate in the hybridization with the 5f electrons (and therefore contribute to their delocalization). The states at the Fermi level are almost completely derived from uranium 5f states, with a small contribution from U 6d and Al 3p states.

When spin polarization and the AF(I) structure is included in the calculation, the spin splitting appears in all shown bands (see Fig. 4(b)). Due to the hybridization with the Al 3p states, the bandwidth of the 6d and 5f electrons in the NM structure is now split in three spin projected sub-bands, two of them occupying the former bandwidth and the third one appearing at higher energies. The population of d and f states of uranium is asymmetric, but the asymmetry is weak in the first case while it is strong in the second one. The U 5f majority spin sub-band below the Fermi energy is almost completely occupied and its bandwidth indicates that the 5f electrons are just as delocalized as the d electrons of U and the p electrons of Al. Whereas, the U 5f minority spin electrons are almost completely excluded from the U sites. The result of this space localized exclusion is an equally localized region of magnetization. We therefore have completely space localized magnetic moments composed of completely itinerant electrons. This non-rigid behavior of the U 5f PDOS is an example of Kübler's covalent magnetism [72]. Fig. 5 shows how the antiferromagnetic coupling between adjacent U atoms is mediated by the p states of its NNN Al(1) and second nearest neighbor Al(2) atoms. The weak asymmetric population of p states in those Al atoms is also reversed [73].

3.1.3. Magnetic anisotropy

Measurements of the magnetic and electrical properties of $NpAl_4$, isomorphic with UAl_4, showed that it is an antiferromagnet with a not simple magnetic structure though the magnetic easy-axis could be along the [010] direction [31]. This magnetic behavior can be associated with non-collinear magnets, having various directions of magnetization along a global quantization axis; which have been known to exist in elemental crystals with coherent helical, spiral, triangular, and canted structures as well as in compounds [74]. Adding this to the background resumed in the Introduction for the magnetic behavior of UAl_4, we investigated the possibility of a non-collinear magnetic lower energy state. The calculations were performed using the primitive cell type AF(I) magnetic structure constraining its cell parameters and fractional atomic coordinates (Table 2), allowing only the magnetic moments to relax. Initially, all the calculations had the starting point chosen with the antiferromagnetic coupling between U^{I} and U^{II} aligned in the $\boldsymbol{z}$ direction while the antiferromagnetic coupling between U^{III} and U^{IV} laid in any position on a cone around the $\boldsymbol{z}$ axis (see Fig. 1 for uranium atoms identification). The opening angle of the cone was varied from 0° to 90°. All these calculations converged to a nearly collinear solution with energy a little higher than the original collinear $\boldsymbol{z}$ direction spin arrangement. The same result was obtained when the starting points were spiral spin structures with null total magnetic moment. This implies that there is no reason to invoke non-collinear spin structure to describe the ground state of UAl_4. Ruled out the possibility of non-collinear magnetism, the following step was to consider the SOC effect on the magnetic

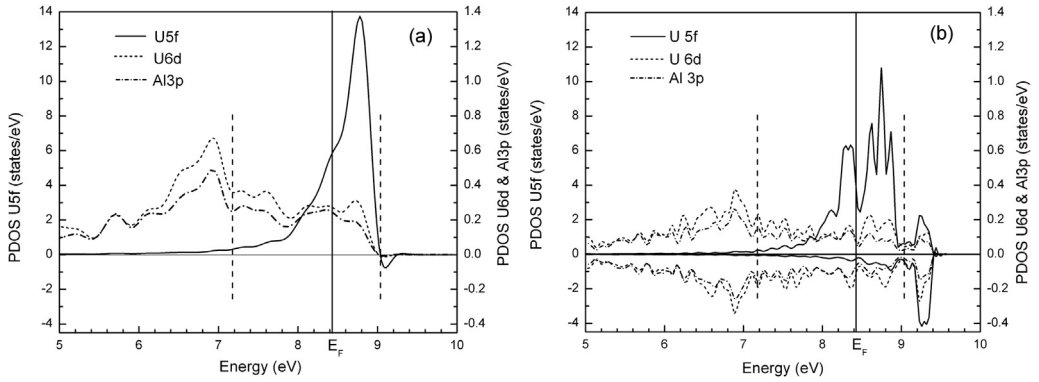

Fig. 4. Calculated site projected DOS on U and Al sites in the nonmagnetic (a) and the antiferromagnetic AF(I) (b) structures of UAl_4. The Fermi level is marked with a vertical solid line.

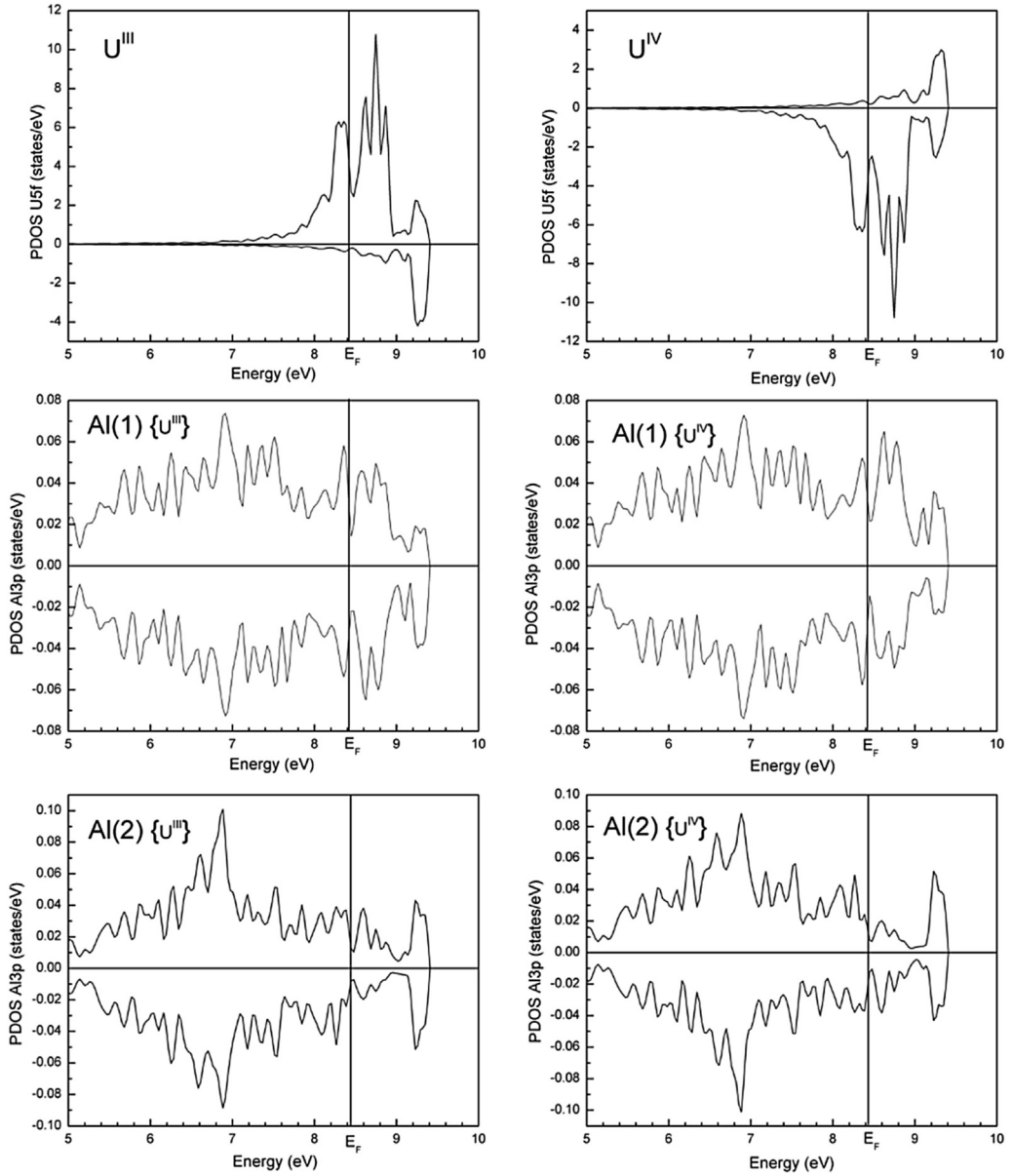

Fig. 5. Calculated site projected DOS on U and Al sites showing how the antiferromagnetic coupling between U^{III} and U^{IV} atoms is mediated by the p states of Al(1) and Al(2).

moment of uranium atoms in the UAl_4 AF(I) structure. This magnetic structure can be seen as a sequence of AF-coupled U $(0\bar{1}1)$ planes (Fig. 6) but the angle between the U spins and the crystal axes was initially unknown for us.

We began the study of the easy axis of magnetization in UAl_4 by estimating the magnetic anisotropy. For this purpose the total energy for three different orientations of the magnetic moment along the ***a***(***x***), ***b***(***y***), and ***c***(***z***) axes of the UAl_4 AF(I) structure was calculated and is shown in Table 4. Total-energy calculations lead to the conclusion that the easy and hard magnetic axes are oriented along the ***b*** and ***a*** axes, respectively. Then, the magnetic anisotropy energy, E_{anis}, was calculated as the difference in the total energies for each orientation and that of the easy magnetic axis. These results are also shown in Table 4. Note that the E_{anis} in the ***a-b*** (001) plane is substantially higher than the E_{anis} in the ***b-c*** (100) plane meaning that the ***b-c*** (100) is the easy magnetization plane.

The spin, orbital, and total magnetic moments for U atoms are also shown in Table 4 for the three fixed directions of spin magnetization. In all cases the spin magnetic moment M_s and the orbital moment M_l are almost antiparallel to each other. Since the modulus of M_l exceeds M_s, the angle between the resultant total magnetic moment M_J and M_s is slightly less than π rad. (180°). In the experimentally relevant case, the spin moment M_s is aligned with the easy ***b*** axis, the modulus of the total magnetic moment M_J is 0.293 μ_B and the angle between M_J and the ***b*** axis is 2.75 rad (157.1°). Opposite directions of the two atomic moments are rather common for the U compounds and appears consistent with the Hund's law for the less than half-filled 5 f shell of the U atom [75]. Unfortunately, there are no neutron diffraction measurements of UAl_4 which could be used to estimate its magnetic structure and the magnetic moment of uranium atoms at low temperature.

It should be noted that the results presented until here do not exclude the possibility of a collinear spin arrangement of lower energy confined to a direction other than the high-symmetry axes. In order to evaluate this possibility we performed the total-energy calculations rotating the magnetization in the ***b-c*** (100) plane. The change in the magnetic anisotropy energy (E_{anis}) with the angle between magnetic moments and the ***b*** axis is shown in Fig. 7(a) for both spin and total magnetizations. The resulting total magnetic moment forms the θ_{total} angle with the ***b*** axis when the spin magnetic moment is aligned at a θ_s angle. The angle $(\theta_{total} - \theta_s)$ between M_J and M_s decreases as the M_s moment approaches the ***c*** axis, with a minimum value of around 2.44 rad (140°) (see Fig. 7(b)). No additional minima in the ***b-c*** (100) plane are found.

In Fig. 7(a) a maximum in E_{anis} is observed for θ_s around 1.05 rad (60°). E_{anis} can be modeled according to [76] by the following equation:

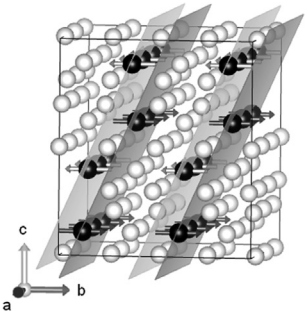

Fig. 6. Crystal structure (six unit cells shown) and predicted magnetic ordering in the AF magnetic ground state for UAl_4 (arrows show the spin orientations). In each set of $(0\bar{1}1)$ planes with antiferromagnetic coupling, the planes are colored with different gray shades.

$$E_{anis} = K_2 \sin^2(\theta_s) + K_4 \sin^4(\theta_s)$$

Second-(K_2) and fourth-(K_4) order magnetic anisotropy constants can be obtained by fitting the angular dependence of the magnetic anisotropy energy by this biquadratic function. This estimate yields for K_2 the value of 0.123 eV and −0.086 eV for K_4. This fairly large absolute value of K_4 could be the reason for the strong reduction of the E_{anis} in the ***b-c*** (100) plane. The maximum obtained in E_{anis} can be understood as originated from the competing constants.

For magnets of low symmetry (orthorhombic, monoclinic, and triclinic), the lowest-order magnetic anisotropy constant depends also on the azimuthal angle φ around the easy magnetic axis [77]:

$$E_{anis} = \left[K_2' + K_2'' \cos 2\varphi\right] \sin^2(\theta_s) + K_4 \sin^4(\theta_s)$$

Where $K_2 = K_2' + K_2''$ with $\varphi = 0$. The constants K_2' and K_2'' can be estimated taking the value of E_{anis} for the ***a*** axis ($\varphi = \pi/2$) from Table 4. We obtain $K_2' = 0.157$ eV and $K_2'' = -0.034$ eV. In order to check our anisotropy-energy expression we calculated it along [111] direction and compared it with the value from DFT calculation, the discrepancy is around 3%. This result allows us to propose the *b* axis as the easy magnetization axis in an UAl_4 antiferromagnetic structure (see Fig. 6).

3.2. Point defects in the UAl_4 crystal

3.2.1. Defect formation energies

Total energies from spin-polarized first principles calculations on the supercells were used to obtain the formation energies of U_mAl_n compounds containing one of the possible constitutional point defects. Formation energy of U_mAl_n compound is calculated as:

$$\Delta E_f(U_mAl_n) = \frac{E_T(U_mAl_n) - mE_T(U) - nE_T(Al)}{m+n}$$

In Fig. 8, the predicted formation energies of off-stoichiometric UAl_4 compounds containing each of the four possible types of constitutional point defects, Al vacancies (Va^{Al}), U vacancies (Va^{U}), Al antisites (Al^{U}) and U antisites (U^{Al}), are plotted. There are eight branches since the three different Al sites according to symmetry are taken into account. The branch giving the lowest formation energy corresponds to the most stable defect structure; Fig. 8 thus shows that the stable constitutional point defects in Al-rich and U-rich o120 UAl_4 are Al antisites (Al^{U}) and U antisites in Al(2) site (U^{Al2}), respectively.

Our interest is focused on aluminum rich side, since experimental reports [4] show that UAl_4 compound widens towards rich aluminum contents. Size effect, together with electronic structure and charge rearrangement on compound forming are responsible for stability. We will discuss these for Al^{U} and Va^{U} in detail below.

3.2.2. Structural relaxations

In order to investigate local effects of the inclusion of defects, we have computed distances between Al atoms and defect positions d_{Al-d} (Table 5). By comparing it with the distance between Al and U position d_{Al-U} in stoichiometric structure, we express relaxation as a percentage of bond length relative to the perfect UAl_4 crystal:

$$\text{Relaxation } (\%) = \frac{d_{Al-d} - d_{Al-U}}{d_{Al-U}} * 100$$

As expected, an inward relaxation of the aluminum nearest neighbor atoms is observed by removing a uranium atom. The

Table 4
Total energy, magnetic anisotropy energy and magnetic moments for U atoms (spin (M_s), orbital (M_l), and total ($M_J = M_s + M_l$)) calculated for three fixed directions of spin magnetization: ***a*** axis [100], ***b*** axis [010] and ***c*** axis [001].

Atom	M_s			M_l			M_J		
	x	*y*	*z*	*x*	*y*	*z*	*x*	*y*	*z*
M_s // *a* axis [100]				**E_{total} (ev) = −119.7660**			**E_{anis} (eV) = 0.1046**		
U^{I}	2.156	0	0	−2.107	0.039	0	0.049	0.039	0
U^{II}	−2.156	0	0	2.106	−0.039	0	−0.050	−0.039	0
U^{III}	2.156	0	0	−2.107	0.039	0	0.049	0.039	0
U^{IV}	−2.156	0	0	2.107	−0.039	0	−0.049	−0.039	0
M_s // *b* axis [010]				**E_{total} (ev) = −119.8706**			**E_{anis} (eV) = 0**		
U^{I}	0	2.211	0	0.096	−2.482	0.054	0.096	−0.271	0.054
U^{II}	0	−2.211	0	−0.097	2.482	−0.054	−0.097	0.271	−0.054
U^{III}	0	2.211	0	0.096	−2.482	0.054	0.096	−0.271	0.054
U^{IV}	0	−2.211	0	−0.096	2.482	−0.054	−0.096	0.271	−0.054
M_s // *c* axis [001]				**E_{total} (ev) = −119.8333**			**E_{anis} (eV) = 0.0373**		
U^{I}	0	0	2.175	0.044	0.096	−2.319	0.044	0.096	−0.144
U^{II}	0	0	−2.175	−0.044	−0.096	2.319	−0.044	−0.096	0.144
U^{III}	0	0	2.175	0.044	0.096	−2.319	0.044	0.096	−0.144
U^{IV}	0	0	−2.175	−0.044	−0.096	2.319	−0.044	−0.096	0.144

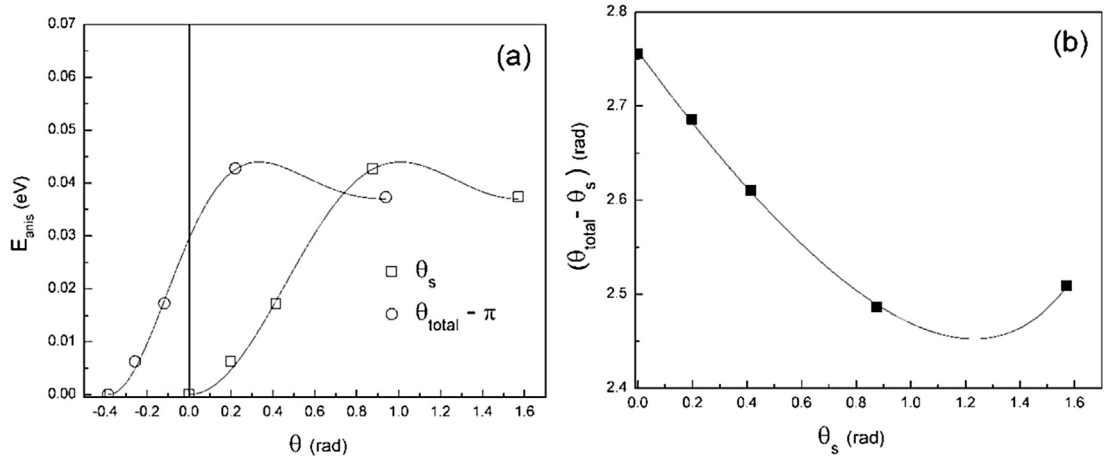

Fig. 7. (a) Magnetic anisotropy energy vs angle θ between the ***b*** axis and the spin (squares) and total magnetization (circles) in the in the ***b***-***c*** plane. The solid line fits the equation $E_{anis} = K_2\sin^2(\theta_s) + K_4\sin^4(\theta_s)$. $\theta_{total-\pi}$ is used instead of θ_{total} for clarity. (b) The angle $(\theta_{total} - \theta_s)$ between the spin and total magnetization as a function of the angle θ between the ***b*** axis and the spin moment.

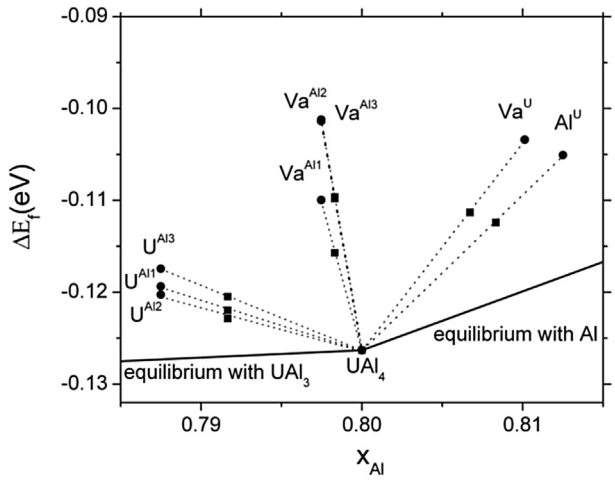

Fig. 8. Energies of formation per atom of the supercells $2 \times 2 \times 1$ (black circles) and $3 \times 2 \times 1$ (black squares) containing one defect. The reference states are pure U in the orthorhombic oC4 structure and pure Al in the cubic cF4 structure.

amount of relaxation follows the same order than the distance

Table 5
Lattice relaxations of the first, second and third nearest neighbor atoms around a defect in UAl_4 crystal. Calculations were performed in the largest supercell ($3 \times 2 \times 1$).

Defect	Distance (d_{Al-d}) aluminum-defect (Å)			Relaxation (%)		
	Al(1)	Al(2)	Al(3)	Al(1)	Al(2)	Al(3)
Va^{U}	2.819	2.950	3.054	−6.687	−4.022	−1.376
Al^{U}	2.985	2.790	2.971	−1.177	−9.232	−4.062

between the uranium vacancy and those neighbor atoms.

When an aluminum atom occupies the uranium site, the structure is also expected to relax inwards the defect position so as to reduce strain energy coming from atomic size misfit between uranium and antisite aluminum atom. A curious effect is observed on Al antisite atom, as a displacement from the original position in the [001] direction towards a (001) plane containing second nearest neighbor Al(2) atoms (Fig. 9). This kind of relaxation reduces the strain among surrounding aluminum atoms and enhances bonding.

3.2.3. Electronic structure

All results shown in this paragraph were obtained with the

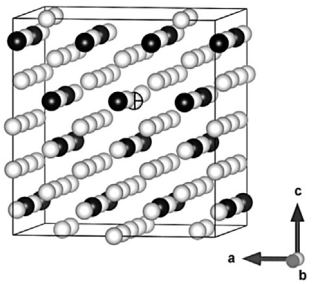

Fig. 9. The marked Al^U antisite is displaced from its original position in UAl_4 compound.

largest supercell ($3 \times 2 \times 1$). Fig. 10 shows BCD plots of aluminum rich structure containing one U vacancy. Compared with the BCD plot of the perfect crystal in Fig. 3, it can be seen that there is a significant spatial redistribution of interstitial bonding charge at Al(1)-Va^U-Al(2), Al(2)-Va^U-Al(3) and Al(3)-Va^U-Al(3) triangular bonding areas around the vacancy. As a result, the Al(1)-Al(2) bonds as well as the U–Al(2) bonds gain electron density. The compensation for these deviations appears as a redistribution of the directional f-bonding charge at the uranium sites around the vacancy, there is a decrease of the charge in the lobes located on the side of the vacancy. The introduction of an Al atom in U site instead of the Va supplies an excess of electrons around the antisite atom leading to the enhancement of the bonds between the neighboring Al atoms and the Al antisite itself (see Fig. 11). The compensation for the deviation from the stoichiometry by the Al antisite in the Al-rich UAl_4 is, therefore, energetically more favorable than that of U vacancy as seen in Fig. 8.

Fig. 12 shows the total DOS of the perfect UAl_4 crystal and the two defect structures. The antiferromagnetism is broken and a non zero magnetic moment in the U 5f bands occurs. Given that the U atom site chosen to introduce the U vacancy had majority U 5f spin up states, one can expect, if these were completely localized electron states, a uniform decrease in the density of states with spin up below the Fermi level while the density of states with spin down is

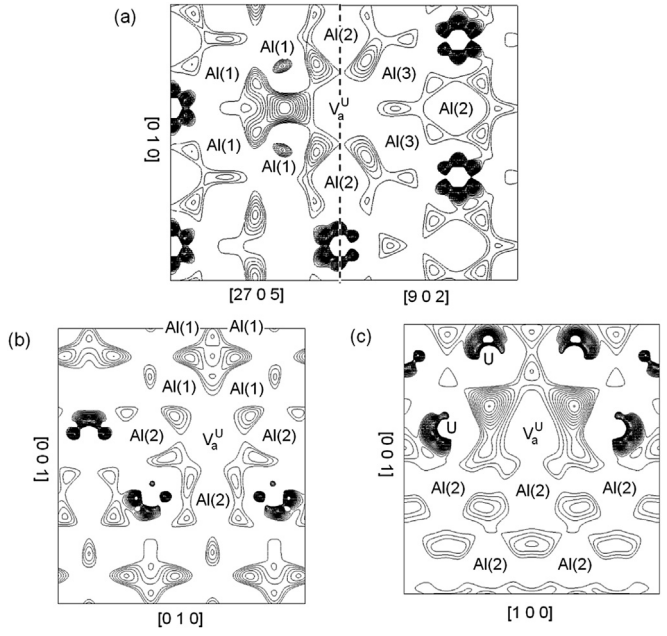

Fig. 10. BCD plot onto selected planes of UAl_4 containing an U vacancy: (a) $(\bar{5}\,0\,27)$ and $(\bar{2}\,0\,9)$; (b) (100); (c) (010). Contourlines are drawn from 1×10^{-3} to 40×10^{-3} electrons/Å^3 with an interval of 1×10^{-3}.

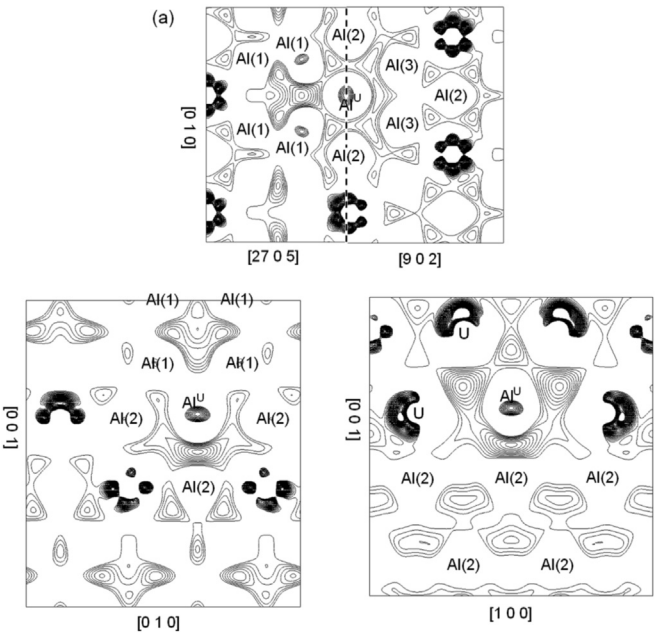

Fig. 11. BCD plot onto selected planes of UAl_4 containing an Al antisite: (a) $(\bar{5}\,0\,27)$ and $(\bar{2}\,0\,9)$; (b) (100); (c) (010). Contourlines are drawn from 1×10^{-3} to 40×10^{-3} electrons/Å^3 with an interval of 1×10^{-3}.

unchanged. Instead of this, there is an increment in the number of U 5f states at energies between 0.2 and 0.6 eV below the Fermi level in both spin directions. We believe that this behavior could be in correspondence with stronger bond states associated to the directional f-bonding charge which, as was already mentioned, undergoes redistribution.

The total DOS of the crystal with Al antisite has two additional peaks in the lower energy part around −1.7 eV below the Fermi level, one for each spin direction. Thus, the appearance of such peaks should be straightforwardly related to the hybridization of the Al 3p and U 6d states coming from the Al antisite and its uranium nearest neighbors.

Analyzing the magnetic moments for each uranium atom in the supercell, we could detect that the most significant changes occur for the uranium atoms located on the set of $(0\bar{1}1)$ planes with antiferromagnetic coupling where the vacancy was introduced (see Fig. 6). Furthermore and considering this antiferromagnetic layer, only the nearest neighbors are affected among all the uranium atoms contained in the sub-layer with the same spin that the vacant site. In the sub-layer with opposite spin direction, an aluminum atom is required to mediate between the vacant site and the affected uranium atom. Fig. 13 shows the site projected PDOS plots of these two different U sites. The dominant features of the PDOS for the U vacancy are the following.

In the nearest neighbors (Fig. 13(a)) not only the f-bonding charge is re-distributed but electrons are lost towards the interstitial charge, and the pseudogap between bonding and antibonding for the U 5f states with spin up moves towards energies higher than the Fermi level, wakening their bondings. On the contrary, the uranium atoms with opposite spin direction respect to the vacant site (Fig. 13(b)) gain electrons from the interstitial charge and redistribute them into in the f-bonding charge. It is interesting to see the effect on these features when the Al atom is introduced in the vacant site to form an antisite. First, in the nearest neighbors (Fig. 13(c)) there is a recovery of electrons from the interstitial charge and of the position of the pseudogap leading to an enhancement in the covalent bond. Second, in Fig. 13(d) the peak close to the Fermi level becomes more prominent and narrow in the

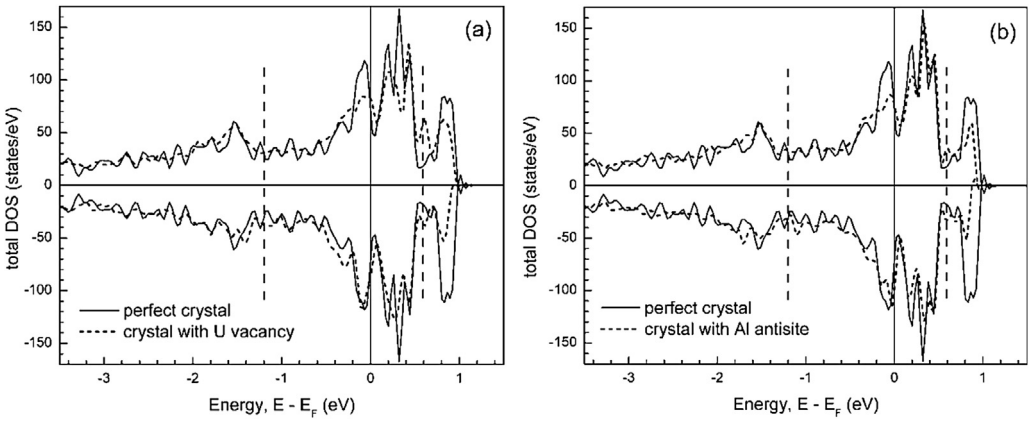

Fig. 12. Total DOS of perfect UAl_4 crystal and of the crystal with two types of point defects in the $3 \times 2 \times 1$ supercell: (a) uranium vacancy Va^U; (b) aluminum antisite Al^U.

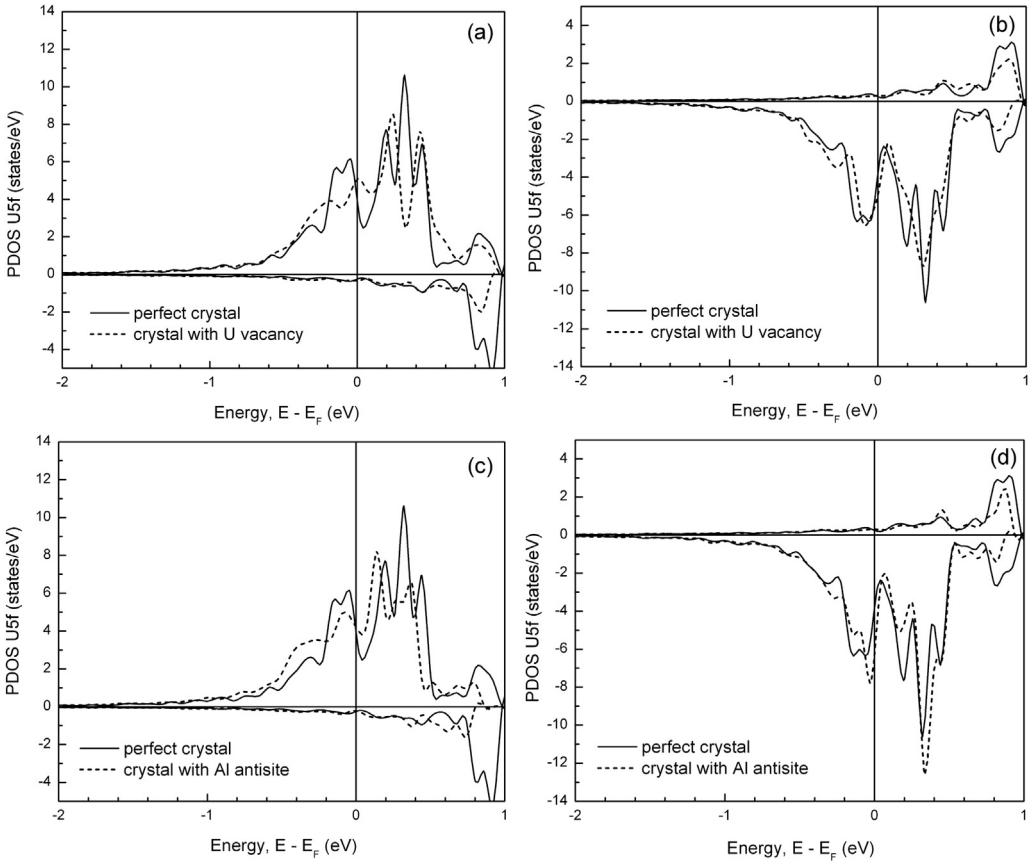

Fig. 13. Site projected DOS on U relevant sites located on the set of $(0\bar{1}1)$ planes with antiferromagnetic coupling in a UAl_4 crystal with defects: (a) and (c) U nearest neighbors to the vacant site or antisite and contained in the sub-layer with the same spin direction than the corresponding to the original defect site; (b) and (d) U nearest neighbors connected through an Al atom to the vacant site or antisite and contained in the sub-layer with spin direction opposite to the corresponding to the original defect site.

PDOS of the uranium atoms with opposite spin direction with respect to the vacant site showing also an increment of the covalent bond between these U atoms and their aluminum nearest neighbors.

4. Conclusions

A study of the point defects in UAl_4 in the DFT-GGA framework using the plane wave pseudopotential method has been undertaken.

As a prerequisite to this research, a magnetic structural study of the UAl_4 orthorhombic crystal structure was performed including SOC. An antiferromagnetic $(0\bar{1}1)$ layer structure with spins aligned to the [010] direction was found to be energetically preferred. SOC was shown to have a significant quenching effect on the spin-moment and to introduce a strong magnetic anisotropy stabilizing the [010] polarization relative to the [001] polarization. The calculated equilibrium volume differs by only 0.7% from the experimental volume; however the axial ratios c/a and c/b are overestimated by 1.5%. The analysis of density of states and bonding

charge density point out that the bonding mechanism consists primarily of band mixing between the U 5f and Al 3p states. The population of f states of uranium is highly asymmetric leading to completely localized magnetic moments composed of entirely itinerant electrons and the antiferromagnetic coupling between adjacent U atoms is mediated by the p states of its neighbor Al atoms.

Tackling the study of point defects in UAl_4, we obtained the formation enthalpies of supercells containing isolated point defects. Our results show that Al antisites and U antisites in Al 4e Wyckoff positions are the constitutional point defects in Al-rich and U-rich oI20 UAl_4, respectively. In this way we have presented here the first set of data which makes it possible to discuss and quantify the point defects concentrations in the experimental composition range for existence of this uranium aluminide.

Defect structures related to relevant experimental compositions were further studied. Both Va^U and Al^U defects induce large inward displacements of the nearest neighbor aluminum atoms and a significant spatial redistribution of interstitial bonding charge at Al–U–Al triangular bonding areas around the defect. The antiferromagnetism is locally broken, a non zero magnetic moment in the U 5f bands occurs mainly for the uranium atoms located in the set of $(0\bar{1}1)$ planes with antiferromagnetic coupling where the defect was introduced.

Acknowledgments

This work was performed in the Gerencia Materiales, CAC – CNEA, and partially founded by the ANPCyT through grant PICT-2011-1861, and by the Universidad Nacional de San Martín through the grant C070 (2013–2014). Part of the calculations was performed in the HPC center at Centro Atómico Constituyentes, Comisión Nacional de Energía Atómica.

References

[1] W. Dienst, S. Nazare, F. Thummler, J. Nucl. Mater. 64 (1977) 1–13.
[2] G.L. Hofman, J. Rest, J.L. Snelgrove, T. Wiencek, S. Koster van Groos, Aluminum-U_3Si_2 interdiffusion and its implications for the performance of highly loaded fuel operating at higher temperatures and fission rates, in: RERTR-1996 International Meeting on Reduced Enrichment for Research and Test Reactors, Seoul, Korea, October 1996. GLHOF296.
[3] M.K. Meyer, G.L. Hofman, S.L. Hayes, C.R. Clark, T.C. Wiencek, J.L. Snelgrove, R.V. Strain, K.H. Kim, J. Nucl. Mater. 304 (2002) 221–236.
[4] S. Balart, L. Kniznik, C. Komar Varela, P.H. Gargano, M. Mirandou, S. Aricó, P.R. Alonso, G.H. Rubiolo, A. Fortis, L. Gribaudo, Current activities in the out of pile investigations of the interaction between UMo and Al or Al alloys, in: RERTR-2009 International Meeting on Reduced Enrichment for Research and Test Reactors, Beijing, China, November 2009. S6-P3.
[5] M.E. Kassner, P.H. Adler, M.G. Adamson, D.E. Peterson, J. Nucl. Mater. 167 (1989) 160–168.
[6] M.I. Mirandou, S.N. Balart, M. Ortiz, M.S. Granovsky, J. Nucl. Mater. 323 (2003) 29–35.
[7] F. Mazaudier, C. Proye, F. Hodaj, J. Nucl. Mater. 377 (2008) 476–485.
[8] L. Kniznik, P.R. Alonso, P.H. Gargano, G.H. Rubiolo, J. Nucl. Mater. 414 (2011) 309–315.
[9] W. Van Renterghem, A. Leenaers, S. Van Der Berghe, Transmission electron microscopy investigation of UAl_x based MTR fuel, in: RRFM-2010 International Topical Meeting on Research Reactor Fuel Management, Marrakesh, Morocco, March 2010, p. 396.
[10] H. Palancher, N. Wieschalla, P. Martin, R. Tucoulou, C. Sabathier, W. Petry, J.F. Berar, C. Valot, S. Dubois, J. Nucl. Mater. 385 (2009) 449–455.
[11] A.K. Chakraborty, R.S. Crouse, W.R. Martin, J. Nucl. Mater. 38 (1971) 93–104.
[12] H.J. Ryu, Y.S. Kim, G.L. Hofman, J. Nucl. Mater. 385 (2009) 623–628.
[13] J. Gan, D.D. Keiser, B.D. Miller, D.M. Wachs, T.R. Allen, M. Kirk, J. Rest, J. Nucl. Mater. 411 (2011) 174–180.
[14] B.S. Borie, Trans. AIME 191 (1951) 800–802.
[15] R. Boucher, J. Nucl. Mater. 1 (1959) 13–27.
[16] O.J.C. Runnalls, R.R. Boucher, Trans. AIME 233 (1965) 1726–1732.
[17] A. Jesse, G. Ondracek, F. Thummler, Powder Metall. 14 (1971) 289–297.
[18] O. Tougait, H. Noël, Intermetallics 12 (2004) 219–223.
[19] P. Chiotti, J.A. Kateley, J. Nucl. Mater. 32 (1969) 135–145.
[20] P. Villars, L.D. Calvert, Pearson's Handbook of Crystallographic Data for Intermetallic Phases 2, American Society for Metals, New York, 1989.
[21] P. Hohenberg, W. Kohn, Phys. Rev. B 136 (1964) 864–871.
[22] W. Kohn, L.J. Sham, Phys. Rev. A 140 (1965) 1133–1138.
[23] C.L. Fu, Y.-Y. Ye, M.H. Yoo, K.M. Ho, Phys. Rev. B 48 (1993) 6712–6715.
[24] P. Blaha, K. Schwarz, G.K.H. Madsen, D. Kvasnicka, J. Luitz, WIEN2k, an Augmented Plane Wave + Local Orbitals Program for Calculating Crystal Properties, Tech. Universität Wien, Karlheinz Schearz, Austria, 2001.
[25] P.R. Alonso, P.H. Gargano, L. Kniznik, L.M. Pizarro, G.H. Rubiolo, Experimental studies and first principles calculations in nuclear fuel alloys for research reactors, in: M.P. Hemsworth (Ed.), Nuclear Materials, Series: Physics Research and Technology, Materials Science and Technologies, Nova Science Publishers, New York, 2011, pp. 47–80.
[26] L. Kniznik, P.R. Alonso, P.H. Gargano, M.D. Forti, G.H. Rubiolo, Procedia Mater. 1 (2012) 514–519.
[27] G. Kresse, J. Hafner, Phys. Rev. B 47 (1993) 558–561;
(a) G. Kresse, Thesis, Technische Universität Wien, Austria, 1993;
(b) G. Kresse, J. Furthmüller, Comp. Mater. Sci. 6 (1996) 15–50;
(c) G. Kresse, J. Furthmüller, Phys. Rev. B 54 (1996) 11169–11186.
[28] D. Sedmidubsky, R.J.M. Konings, P. Soucek, J. Nucl. Mater. 397 (2010) 1–7.
[29] L. Kniznik, P.R. Alonso, P.H. Gargano, G.H. Rubiolo, First-principles study of constitutional point defects in oI20 UAl_4, in: RERTR-2011 International Meeting on Reduced Enrichment for Research and Test Reactors, Santiago, Chile, October 2011. S12-P10.
[30] A. Mielke, W.W. Kim, G. Fraunberger, G.R. Stewart, J. Alloys Compd. 189 (1992) 123–125.
[31] D. Aoki, Y. Haga, Y. Homma, Y. Shiokawa, E. Yamamoto, A. Nakamura, R. Settai, Y. Onuki, J. Phys. Soc. Jpn. 78 (2009) 044712/1–044712/7.
[32] K. Kadowaki, S.B. Woods, Solid State Commun. 58 (1986) 507–509.
[33] K.H.J. Buschow, H.J. van Daal, AIP Conf. Proc. 5 (1972) 1464–1477.
[34] E. Burzo, P. Lucaci, I. Lupsa, J. Magn. Magn. Mater. 140–144 (1995) 1413–1414.
[35] I. Lupsa, P. Lucaci, O. Garlea, E. Burzo, Phys. Status Solidi A Appl. Res. 199 (2003) 294–298.
[36] T. Gouder, Surf. Sci. 382 (1997) 26–34.
[37] A.M. Boring, R.C. Albers, G.R. Stewart, Phys. Rev. B 31 (1985) 3251–3259.
[38] R.A. de Groot, D.D. Koelling, M. Weger, Phys. Rev. B 32 (1985) 2659–2662.
[39] N.V. Chandra Shekar, P.Ch. Sahu, M. Rajagopalan, M. Yousuf, K. Govinda Rajan, J. Phys. Condens. Matter 9 (1997) 5867–5874.
[40] Y. Tatetsu, H. Teruya, S. Shirono, T. Maehira, J. Phys. Soc. Jpn. 80 (2011). SA126/1–SA126/3.
[41] S. Kang, T. Gao, X. Tian, Phys. B 407 (2012) 748–755.
[42] J.-P. Crocombette, F. Jollet, T. Nga, T. Petit, Phys. Rev. B 64 (2001) 1041071–10410712.
[43] M. Freyss, T. Petit, J.-P. Crocombette, J. Nucl. Mater. 347 (2005) 44–51.
[44] F. Gupta, G. Brillant, A. Pasturel, Philos. Mag. 87 (2007) 2561–2569.
[45] P. Nerikar, T. Watanabe, J.S. Tulenko, S.R. Phillpot, S.B. Sinnott, J. Nucl. Mater. 384 (2009) 61–69.
[46] B. Dorado, J. Durinck, P. Garcia, M. Freyss, M. Bertolus, J. Nucl. Mater. 400 (2010) 103–106.
[47] P.E. Blöchl, Phys. Rev. B 50 (1994) 17953–17979.
[48] J.P. Perdew, K. Burke, M. Ernzerhof, Phys. Rev. Lett. 77 (1996) 3865–3868.
[49] D. Hobbs, G. Kresse, J. Hafner, Phys. Rev. B 62 (2000) 11556–11570.
[50] J. Kübler, K.H. Höck, J. Sticht, A.R. Williams, J. Phys. F. Met. Phys. 18 (1988) 469–483.
[51] K. Momma, F. Izumi, J. Appl. Crystallogr. 44 (2011) 1272–1276.
[52] J.K. Lang, Y. Baer, Rev. Sci. Instrum. 50 (1979) 221–226.
[53] J.K. Lang, Y. Baer, P.A. Cox, J. Phys. F. 11 (1981) 121–138.
[54] P.A. Cox, J.K. Lang, Y. Baer, J. Phys. F. 11 (1981) 113–119.
[55] Y. Baer, J. Schoenes, Solid State Commun. 33 (1980) 885–888.
[56] O. Gunnarsson, D.D. Sarma, F.U. Hillebrecht, K. Schönhammer, J. Appl. Phys. 63 (1988) 3676–3679.
[57] S.L. Dudarev, D. Nguyen Manh, A.P. Sutton, Philos. Mag. B 75 (1997) 613–628.
[58] S.L. Dudarev, G. Botton, S.Y. Savrasov, C.J. Humphreys, A.P. Sutton, Phys. Rev. B 57 (1998) 1505–1509.
[59] A.D. Becke, J. Chem. Phys. 98 (1993) 1372–1377.
[60] J.P. Perdew, M. Ernzerhof, K.J. Burke, J. Chem. Phys. 105 (1996) 9982–9985.
[61] Y. Baer, J.K. Lang, Phys. Rev. B 21 (1980) 2060–2062.
[62] J. Yu, R. Devanathan, W.J. Weber, J. Phys. Condens. Matter 21 (2009) 435401 (10pp).
[63] W. Xie, W. Xiong, C.A. Marianetti, D. Morgan, Phys. Rev. B 88 (2013) 235128 (22pp).
[64] J.W. Allen, S.J. Oh, L.E. Cox, W.P. Ellis, M.S. Wire, Z. Fisk, J.L. Smith, B.B. Pate, I. Lindau, A.J. Arko, Phys. Rev. Lett. 54 (1985) 2635–2638.
[65] N.V. Chandra Shekar, P.Ch. Sahu, V. Kathirvel, S. Chandra, Indian J. Phys. 86 (2012) 971–976.
[66] A. Lindbaumy, J. Hafner, E. Gratzy, S. Heathman, J. Phys. Condens. Matter 10 (1998) 2933–2945.
[67] J.-S. Kang, J.W. Allen, M.B. Maple, M.S. Torikachvili, B. Pate, W. Ellis, I. Lindau, Phys. Rev. Lett. 59 (1987) 493–496.
[68] P.Ch. Sahu, N.V. Chandra Shekar, Pramana J. Phys. 54 (2000) 685–708.
[69] D.D. Koelling, B.D. Dunlop, C.W. Crabtree, Phys. Rev. B 31 (1985) 4966–4971.
[70] V.G. Tsirelson, R.P. Ozerov, J. Mol. Struct. Theochem 255 (1992) 335–392.
[71] C.D. Gelatt, A.R. Williams, V.L. Moruzzi, Phys. Rev. B 27 (1983) 2005–2013.
[72] A.R. Williams, R. Zeller, V.L. Moruzzi, C.D. Gelat, J. Kübler, J. Appl. Phys. 52 (1981) 2067–2069.
[73] V.A. Gubanov, A.I. Liechtenstein, A.V. Postnikov, Magnetism and the Electronic

Structure of Crystals, Springer-Verlag, Berlin, 1992.
[74] H. Yamagami, Phys. Rev. B 61 (2000) 96246–96256.
[75] M.S.S. Brooks, O. Eriksson, L. Severin, B. Johansson, Phys. B 192 (1993) 39–49.
[76] A.B. Shick, Phys. Rev. B 65 (2002) 1805091–1805904.
[77] R. Skomski, J. Zhou, Nanomagnetic models, in: D. Sellmyer, R. Skomski (Eds.), Advanced Magnetic Nanostructures, Springer Science+Business Media Inc, New York, 2006, pp. 41–90.